

Pix2Repair: Implicit Shape Restoration from Images

Nikolas Lamb, Sean Banerjee, Natasha Kholgade Banerjee

Clarkson University, Potsdam NY, USA

{lambne, sbanerje, nbanerje}@clarkson.edu

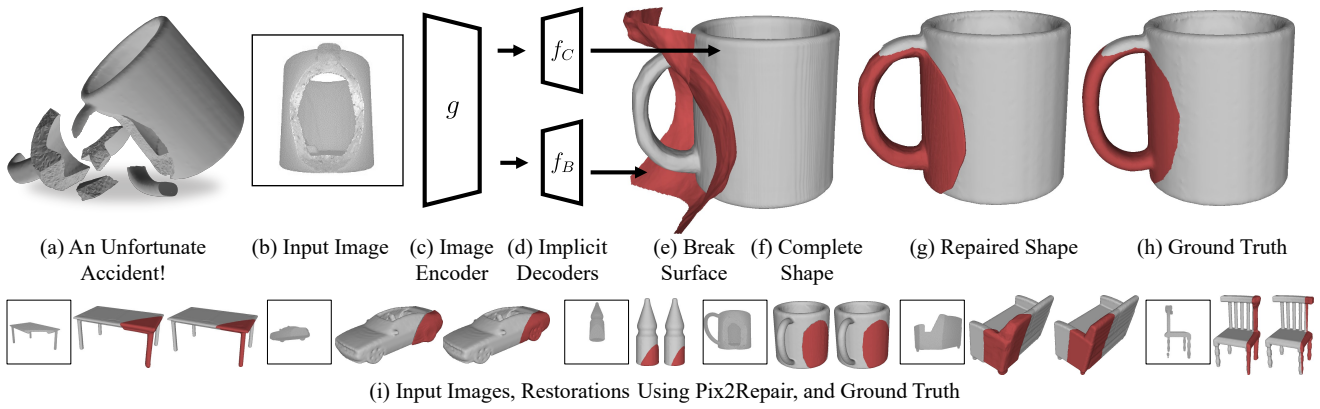


Figure 1: We present Pix2Repair, an automated shape repair approach. Pix2Repair takes an image of a fractured object as input and predicts a complete shape and break surface, which combine to generate a restoration shape.

Abstract

We present *Pix2Repair*, an automated shape repair approach that generates restoration shapes from images to repair fractured objects. Prior repair approaches require a high-resolution watertight 3D mesh of the fractured object as input. Input 3D meshes must be obtained using expensive 3D scanners, and scanned meshes require manual cleanup, limiting accessibility and scalability. *Pix2Repair* takes an image of the fractured object as input and automatically generates a 3D printable restoration shape. We contribute a novel shape function that deconstructs a latent code representing the fractured object into a complete shape and a break surface. We show restorations for synthetic fractures from the Geometric Breaks and Breaking Bad datasets, and cultural heritage objects from the QP dataset, and for real fractures from the Fantastic Breaks dataset. We overcome challenges in restoring axially symmetric objects by predicting view-centered restorations. Our approach outperforms shape completion approaches adapted for shape repair in terms of chamfer distance, earth mover’s distance, normal consistency, and percent restorations generated.

1. Introduction

Many people know the frustration of trying to repair a treasured glass, vase, or mug that has been accidentally fractured, e.g., Figure 1(a). Sometimes fractured objects can be repaired via reassembly. However, in many cases parts are destroyed or lost during the fracturing process leaving gaps in the repaired object. Automated shape repair approaches seek to fill this gap by automatically generating restoration shapes for fractured objects. In addition to preserving heirlooms, object repair algorithms have the potential to reduce household waste, restore cultural heritage objects, and automate industrial recycling. A recent body of work has emerged to automate the repair of fractured objects by predicting 3D printable restoration shapes using machine learning [12, 21, 20, 19]. However existing approaches operate in low resolution voxel space [12], or require high resolution 3D scans of the fractured object [21, 20, 19] which must be obtained using expensive scanners, e.g. the \$2,000 Einscan-SP, making them inaccessible to consumers.

We present *Pix2Repair*, an approach to automatically generate repair parts for fractured objects from images. Our approach builds on prior approaches that perform shape completion from images using implicit representations [33, 25, 31, 4, 48, 24, 56, 14]. However, existing shape com-

pletion approaches generate a complete shape from a partial observation, e.g., an image that observes the complete shape from a fixed perspective. Different from shape completion, our approach generates a restoration shape from an image of a fractured object, such as the image shown in Figure 1(b). Generating restoration shapes is a harder task than generating complete shapes as restorations are often much smaller than complete shapes, as is the case for the restoration shape in Figure 1(g). Restorations also contain high-frequency geometry at the point of fracture, as shown in Figure 1(b), that is difficult to predict directly.

To overcome the challenge of representing shapes with small size and high frequency surface detail, we compute the repair shape as the Boolean intersection of a predicted complete shape and break shape, where the break shape is given by a break surface, shown in Figures 1(f) and (e) respectively. Our approach draws inspiration from existing shape repair approaches [20, 19], which similarly represent the restoration shape as a Boolean intersection. However, our approach learns to predict a complete shape and break surface from a single shape code representing the fractured object, in contrast to prior approaches that obtain two separate complete and break codes by performing iterative optimization during inference. Learning a mapping from the fractured shape code to the complete shape and break surface allows our network to predict restoration shapes directly from color images of the fractured shape. Accepting images as input makes Pix2Repair more accessible to consumers and faster during inference than prior approaches. We make the following contributions:

1. We present the first approach to generate implicit restoration shapes from color images.
2. We introduce a novel network architecture that learns a mapping directly from a fractured shape code to a complete shape and break surface.
3. We demonstrate the generalizability of our approach by showing repairs for fractured objects from three synthetic fracture datasets, and one physically fractured dataset of real-world fractured objects.

We perform training using synthetically fractured objects from Geometric Breaks [19], which is derived from ShapeNet [3]. We evaluate our approach on synthetically fractured objects from Breaking Bad [41] and synthetically fractured objects in the style of ancient Greek pottery from the QP Cultural Heritage Objects dataset [17]. We also test Pix2Repair on 100 physically fractured and scanned objects from the Fantastic Breaks dataset [22]. We overcome ambiguous restoration shape pose for axially symmetric objects by predicting restoration shapes in the camera frame instead of the object frame. We outperform three shape completion approaches that we adapt for shape repair in

terms of chamfer distance, earth mover’s distance, normal consistency, and percent of restorations generated.

2. Related Work

2.1. Shape Repair

Prior work in shape repair has been mostly manual, with approaches only repairing a single object, e.g. a terracotta artifact [39], a silver crown [40], a fruit bowl [1], a dinosaur vertebrae [38], a rhinoplasty implant [2], or a dental prosthesis [37]. Manual approaches require that the user generate all or part of the restoration using 3D design software, which is out of the scope of the average consumer. Some automated approaches generate repairs by exploiting object symmetry, i.e. using symmetric reflection and subtraction [44, 23, 30], or performing shape subtraction with a high-resolution oracle [18]. However, these approaches fail to repair asymmetric objects [44, 23, 30], or cannot repair objects without a corresponding complete 3D scan [18].

Early machine learning based repair approaches operate in 32^3 voxel space [12], generating coarse repair parts that cannot accurately represent the complex fractured surface. More recent work in shape repair [20, 21, 19] uses the autoencoder framework introduced by DeepSDF [34]. These approaches generate restoration shapes by learning a mapping from fractured shapes to restoration shapes [21], or learn occupancy [20] or combined signed distance, occupancy, and normal field functions [19] for a complete shape and break surface that combine to generate the restoration shape. Similar to prior approaches [19, 20], our approach represents the restoration shape as a Boolean intersection. However, unlike prior work our shape functions take a latent code corresponding to the fractured shape as input, instead of two separate codes for the complete shape and break surface. By inputting a single fractured shape code, our approach learns to map fractured shape observations to complete shapes and break surfaces, allowing us to perform inference directly from color images of the fractured shape.

2.2. Shape Completion

A related but still disparate field of study from shape repair is shape completion, which focuses on generating a complete shape from a color image. Recent work in shape completion from images can be categorized according to the method of shape representation. Some approaches perform completion on point clouds [35, 58, 51, 28], which are compact and are easy to obtain, e.g., using depth cameras. However, as point clouds lack orientable surfaces they cannot be used to generate 3D-printable restoration parts. Though mesh based approaches [42, 9, 47, 10, 50, 46] produce closed, orientable surfaces that are necessary to represent physically realizable restoration shapes, they struggle to represent shapes of arbitrary topology or overly com-

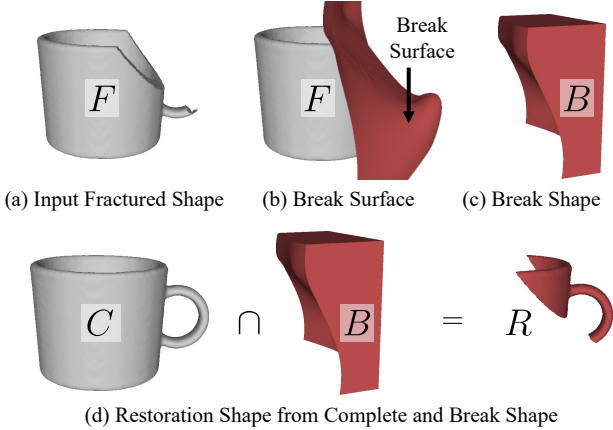


Figure 2: (a) Given a fractured shape F , (b) the break surface intersects with F at the point of fracture, (c) and the break shape B is the point set on the restoration side of the break surface. (d) The union of the complete shape C and break shape B gives the restoration shape R .

plex meshes [31]. Voxel approaches have been extensively studied for shape representation, including large-scale scene reconstruction [36], single and multi-view object completion [5, 54, 55], and completion from 2.5D images [49]. Recent work has improved the efficiency of voxel approaches using, e.g., sparse convolutions [6, 57] and hierarchical models [6, 53]. However, despite advancements in efficiency, voxel approaches still discretize the output space, limiting their ability to represent the high-frequency geometry present at the fractured region of restoration shapes.

A large body of recent work has focused on learning to represent shapes implicitly using functions [33, 25, 31, 4, 48, 24, 56, 14]. Shape functions can reconstruct shapes at arbitrarily high resolutions, making them well suited for restoration shape prediction. Occupancy networks [31] was one of the first approaches to explore using the parameterized occupancy function to perform single-view reconstruction. Later approaches would propose modifications to shape functions such as learning multi-scale implicit fields [48], disentangling object geometry and texture [24], imposing symmetry constraints [56], or learning to deform shape templates [14]. Unlike prior shape completion approaches, our approach learns to predict a restoration shape as the Boolean intersection of two other shape functions, i.e. the complete shape and break surface. In Section 6 we demonstrate that by representing the restoration shape as a Boolean intersection, our approach outperforms shape completion approaches that are adapted to perform shape repair in terms of the chamfer distance, earth mover’s distance, normal consistency, and percent of restorations generated.

3. Representing Restoration Shapes

The goal of our approach is to generate a restoration shape from an image of the fractured shape, such that the restoration shape can be used to repair the fractured shape. We represent shapes as open point sets. We represent the occupancy of a point \mathbf{x} in a given shape $S \in \{C, F, R\}$ as $o_S(\mathbf{x})$, such that $o_S(\mathbf{x}) = 1$ if $\mathbf{x} \in S$ and $o_S(\mathbf{x}) = 0$ otherwise, where C , F , and R refer to the complete, fractured, and restoration shapes respectively. We define the break surface, shown in Figure 2(b), as a 2D manifold that intersects the fractured and restoration shapes at the point of fracture. We define the break shape B , shown in Figure 2(c), as the set of points on the restoration side of the break surface, i.e. $o_B(\mathbf{x}) = 1$ if \mathbf{x} is on the restoration side of the break surface and $o_B(\mathbf{x}) = 0$ if \mathbf{x} is on the fractured side of the break surface. Though the break shape extends infinitely out from the fractured shape, in practice we limit it to the unit cube. We use an open set representation to prevent points from belonging to F and R simultaneously.

Using the definition for B , the restoration shape can be represented in terms of the complete shape and break shape as $R = C \cap B$. We show an example restoration shape obtained through the intersection of a complete and break shape in Figure 2(d). We follow the approach of Lamb et al. [20] to obtain R using the occupancy function definitions for C and B . We obtain the occupancy equation for R in terms of a given point \mathbf{x} as $o_R(\mathbf{x}) = o_C(\mathbf{x}) \wedge o_B(\mathbf{x})$, where \wedge represents the logical and operator. To enable $o_R(\mathbf{x})$ to work with continuous values, i.e. to be used in a loss function, we relax the equation for $o_R(\mathbf{x})$ using the product T-norm [11], such that

$$o_R(\mathbf{x}) = o_C(\mathbf{x})o_B(\mathbf{x}). \quad (1)$$

Equation 1 allows us to obtain the occupancy for R in terms of the predicted occupancy for C and B .

4. Pix2Repair

We learn two functions, f_C and f_B , to represent occupancy in the complete shape and occupancy in the break shape respectively. During training, the function f_C is tasked with learning a one-to-many mapping from the fractured shape observation to the complete shape. The function f_B is tasked with learning a one-to-one mapping from the fractured shape observation to the break shape. Each function takes point $\mathbf{x} \in \mathbb{R}^3$ as input and is conditioned on a latent code corresponding to an observation of the fractured shape \mathbf{z} , such that $o_C(\mathbf{x}) = f_C(\mathbf{z}, \mathbf{x})$ and $o_B(\mathbf{x}) = f_B(\mathbf{z}, \mathbf{x})$. During training and testing we obtain \mathbf{z} by passing an input image through an image encoder g to obtain a fractured shape latent code. We compute occupancy in the restoration shape by substituting the predicted values into Equation 1, i.e. as $o_R(\mathbf{x}) = f_B(\mathbf{z}, \mathbf{x})f_C(\mathbf{z}, \mathbf{x})$.

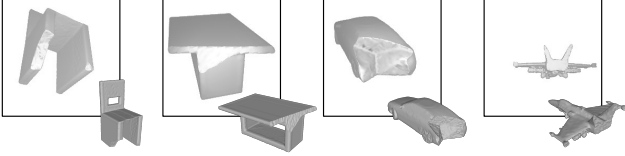


Figure 3: Fracture renders of Geometric Breaks objects.

We train our network on complete, break, and restoration shape tuples (C, B, R) . We use $\hat{o}_C(\mathbf{x})$, $\hat{o}_B(\mathbf{x})$, and $\hat{o}_R(\mathbf{x})$ to denote the ground truth occupancy values for shapes C , B , and R respectively at a point \mathbf{x} . During training, for each shape tuple we optimize with respect to the loss

$$\mathcal{L} = \sum_{\mathbf{x} \in \mathcal{X}} (\mathcal{L}_C + \lambda_B \mathcal{L}_B + \lambda_R \mathcal{L}_R), \quad (2)$$

where

$$\mathcal{L}_C = BCE(o_C(\mathbf{x}), \hat{o}_C(\mathbf{x})), \quad (3)$$

$$\mathcal{L}_B = BCE(o_B(\mathbf{x}), \hat{o}_B(\mathbf{x})), \text{ and} \quad (4)$$

$$\mathcal{L}_R = BCE(o_R(\mathbf{x}), \hat{o}_R(\mathbf{x})). \quad (5)$$

In Equations (4), (5), and (5), BCE is the binary cross-entropy loss, and \mathcal{X} is a set of probing points. The losses \mathcal{L}_C , \mathcal{L}_B , and \mathcal{L}_R encourage the predicted values for the complete, break, and restoration shapes to converge to the ground truth values during training. λ_B and λ_R are coefficients that allow us to balance the relative importance of the complete, break, and restoration shape loss.

During training we optimize with respect to the parameters of g , f_C , and f_B . We use $\lambda_B = 1.0$ and $\lambda_R = 1.0$. To perform optimization we use the Adam [16] optimizer with a learning rate of $lr = 2e-4$. For all experiments we train our approach for 600 epochs.

Unless otherwise specified we use ResNet34 as our image encoder g . We concatenate ResNet34 with a fully connected layer with 512 output nodes to obtain a 512 dimensional fractured shape code \mathbf{z} . We represent the occupancy functions f_C and f_B using two neural networks with 6 ResNet blocks and batch normalization [15]. Each ResNet block has 256 nodes with leaky ReLU activation functions. The latent code and points are input to f_C and f_B separately using two fully connected layers with 256 output nodes and added together after the first layer. The final layer has a single output node with a sigmoid activation function. For view-centered fractured shape restoration, we use ResNet18 as our image encoder g , and 5 ResNet blocks for f_C and f_B .

To obtain sample points for training, for each training shape tuple we pre-compute n sample points uniformly in a cube with side lengths of 1.1 units surrounding the shapes. We also pre-compute n sample points on the surface of each shape in the tuple, and offset the surface points randomly according to a Gaussian distribution with $\sigma = 0.01$. We

combine the uniform and surface sampled points into a single set \mathcal{P} . We use $n = 50,000$. On each training iteration we randomly select a subset $\mathcal{X} \subset \mathcal{P}$ of m sample points from the pre-computed uniform and surface sampled points. We select the points \mathcal{X} such that, for each shape $S \in \{C, B, R\}$, at least $\frac{m}{6}$ points lie inside of S and at least $\frac{m}{6}$ points lie outside of S . During training, we use $m = 2,048$ sample points. After training our network, to obtain the restoration mesh we query our network with a grid of k^3 points and extract the 0.5 level isosurface using marching cubes [27]. For evaluation we use $k = 128$. For the visualizations shown in the paper we use $k = 256$.

5. Data Preparation

We train our approach on synthetically fractured objects from the Geometric Breaks dataset [19], and evaluate our approach on four fractured object datasets.

Geometric Breaks. The dataset contains 24,102 synthetically fractured objects from the jars, bottles, mugs, airplanes, chairs, cars, sofas, and tables classes from ShapeNet [3]. Fractured objects are generated by subtracting a complete object with a randomized geometric primitive. The Geometric Breaks dataset contains ground truth complete, break, and restoration shapes. We split the dataset 70%/10%/20% into train, validation, and test sets. To prevent class imbalances between training and testing, we perform the train, validation, and test splitting within each class. We use a total of 16,962 objects for training, 2,420 objects for validation, and 4,720 objects for testing.

Breaking Bad. The Breaking Bad [41] dataset contains 1,047,400 synthetically fractured objects from PartNet [32] and Thingi10K [59]. The objects are fractured into 80 common fracture modes using physical simulation, sometimes resulting in many small fractured parts. To ensure that fractured objects are reasonably large, we only use fractures that contain two parts, and select the larger part as the fractured object. We randomly select 1,000 out of the 12,939 everyday objects that contain two parts for evaluation.

QP Dataset. The QP Cultural Heritage Objects [17] dataset contains objects computer modeled in the style of ancient Greek pottery. We waterproof and synthetically fracture the objects using the same method as Geometric Breaks. We use the 332 objects that are successfully waterproofed and fractured for evaluation.

Fantastic Breaks. The Fantastic Breaks [22] dataset contains 150 physically fractured and 3D scanned objects. The dataset contains common household objects such as mugs, jars, plates, bowls, and figurines, with ground truth restoration parts. We compute ground truth break surfaces for the objects using the same method as Geometric Breaks. We use 100 randomly selected objects for evaluation.

We generate renders that look directly at the fractured region. We follow prior work that trains on synthetic ren-

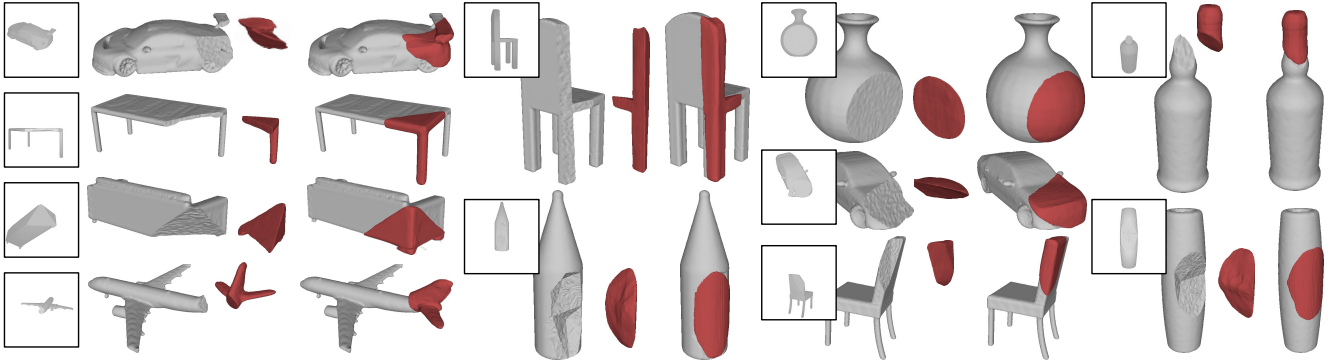


Figure 4: Restoration shapes for objects from the Geometric Breaks dataset. For each object, the input image is on the left, the fractured object with restoration shape opened to show the fractured region is in the middle, and the repaired object is on the right. Fractured objects are shown in gray, restorations are shown in red.

ders [14, 4, 13, 31], as no publicly available image dataset of fractured objects currently exists. We show example renders in Figure 3. To create renders, we compute the volumetric center of all vertices on the fractured region. We place a camera looking at the center of the fractured region vertices. We fit a plane to the fractured region vertices, and offset the camera in the direction of the plane normal. The normal may be pointing in the incorrect direction, i.e. pointing into the fractured object. To prevent incorrect normals, we compute the average dot product between the normal and the set of vectors pointing from the center of the fractured region vertices to the vertices in the fractured object, and flip the normal if the dot product is positive. We offset the camera in the direction of the normal such that it observes the entire object. We light the object using ambient lighting and using a camera-centered spotlight. We render objects at 224x224 pixel resolution using Pyrender [29].

6. Results

We show results using Pix2Repair to generate restorations for objects from the Geometric Breaks dataset in Figure 4. Our approach is able to restore complex missing components such as the tail of the airplane on the left of Figure 4. Our approach restores fractured parts from challenging viewpoints that partially obscure the intact part of the fractured object, e.g. the table and sofa on the left of Figure 4. Unlike approaches based on symmetry, we can repair objects with symmetrical fractures, such as the airplane on the left and the car and the bottle on the right of Figure 4.

To evaluate predicted restoration shapes we use the chamfer distance (CD) as defined by Park et al. [34]. CD is an indicator of overall shape similarity, but may fail to capture out-of-distribution predictions [52]. A challenge of predicting canonically oriented restoration shapes is that the pose of the restoration shape cannot be determined for objects with rotational symmetry, e.g. the bottle in the mid-

dle of Figure 4. As the location of the fractured region is independent of the object’s canonical orientation, the network cannot accurately estimate where the restoration shape should be placed relative to the canonically oriented fractured shape. To evaluate symmetric shapes, we rotate the restoration shape around the up-axis x times, and take the rotation that minimizes the chamfer distance between the predicted restoration shape and the ground truth shape to be the pose of the predicted restoration shape. For the mugs, bottles, and jars classes we use $x = 36$. For the tables class we use $x = 4$, as tables often have two perpendicular planes of symmetry. For success the CD should be low.

We also evaluate shapes using the normal consistency (NC) as defined by Mescheder et al. [31], and the earth-mover’s distance (EMD) as defined by Liu et al. [26]. NC captures the alignment of surface normals between the predicted and ground truth shapes. EMD penalizes out of distribution samples, but is insensitive to fine-structured local details [52]. For success, EMD should be low and NC should be high. For all approaches we also show the non-zero percent (NZ%). NZ% denotes the percentage of fractured shapes for which a restoration shape is generated, i.e. for which the occupancy is not predicted as all zero. We use the EMD implementation by Liu et al. [26], over 4,096 sample points. We compute CD and NC over 30,000 points.

6.1. Repair Generalizability

We demonstrate the generalizability of our approach to objects from other datasets in Figure 5. We train our approach for 600 epochs on the Geometric Breaks dataset and test on objects from Breaking Bad, from Fantastic Breaks, and on QP Cultural Heritage objects. Breaking Bad contains everyday objects such as cups, bowls, and plates. As shown in Figure 5(a), our approach is able to restore a variety of kitchenware objects from Breaking Bad, as they are similar in form to the mugs, jars, and bottles classes

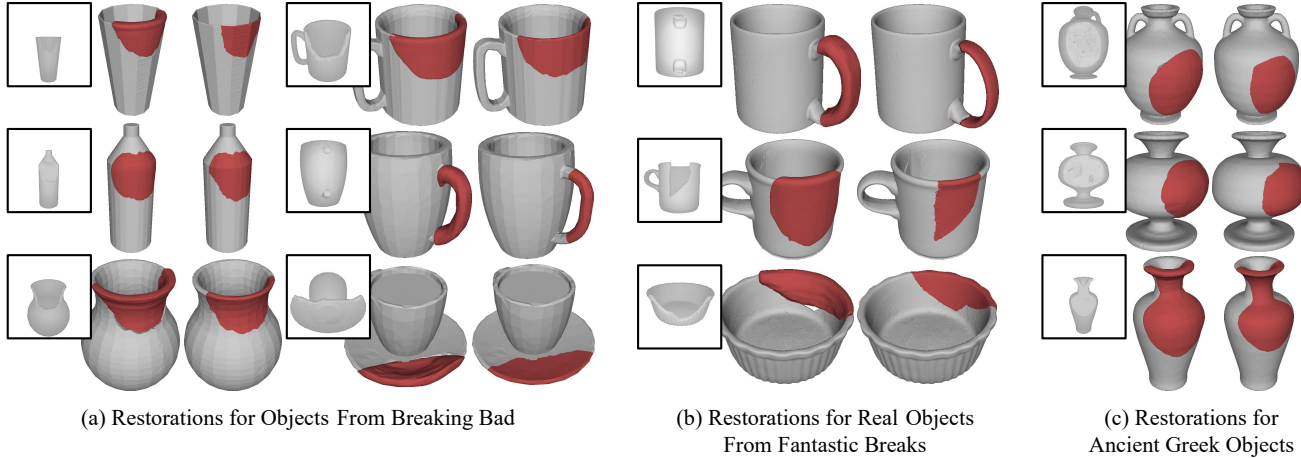


Figure 5: Restorations using Pix2Repair for (a) synthetically fractured objects from Breaking Bad, (b) real physically fractured objects from Fantastic Breaks, and (c) objects from the QP dataset. Restoration on the left, ground truth on the right.

Dataset	CD	NC	NZ%
Geometric Breaks	0.0308	0.7033	99.85%
Breaking Bad	0.1553	0.5604	99.40%
Fantastic Breaks	0.0728	0.6372	100.00%
QP Dataset	0.0146	0.5919	99.70%

Table 1: Chamfer distance (CD), normal consistency (NC), and non-zero percent (NZ%) over fractured object datasets.

from ShapeNet. In Figure 5(b), we show restorations generated using Pix2Repair on physically fractured objects from Fantastic Breaks. Our approach is still able to generate reasonable restorations for common household objects such as mugs and bowls, despite being trained exclusively on synthetically fractured objects. We also show restorations for cultural heritage objects modeled in the style of ancient Greek pottery. In Figure 5(c), we show restorations for a Greek Amphora, Psykter, and a Greek vase. Though Pix2Repair is trained on modern objects, it generates feasible restorations for cultural heritage objects, showing promise to automatically repair archaeological artifacts.

In Table 1 we show metrics over each of the four datasets we use to evaluate our approach. For objects from Breaking Bad we compute the single-sided chamfer distance and normal consistency, i.e. the distance and dot product from every sampled point and normal in the restoration to the nearest sampled point and normal in the ground truth, as ground truth Breaking Bad objects have extraneous interior geometry. In comparison to the Geometric Breaks dataset, the Breaking Bad dataset is more challenging, with a CD of 0.1553 compared to 0.0308. Though our approach is able to repair a large number of kitchenware objects from Breaking Bad, as shown in Figure 5(a), the dataset also contains a large number of uncommon objects such as sculptures, toys,

and other complex objects that are not present in Geometric Breaks. Breaking Bad also contains many simple objects that, when fractured and rendered, do not provide enough information to enable repair. An example is given in Section 7. Pix2Repair also generates accurate repairs for real fractured objects, with a chamfer of 0.0728 and a 100% generation rate, and for cultural heritage objects with a chamfer of 0.0146. Given the low CD and EMD when restoring real objects, using Pix2Repair for real object restoration is especially promising as a direction for future work.

6.2. Comparison to Shape Completion

As no image-based shape repair approaches exist, we adapt three existing shape completion approaches to perform shape repair. We compare to IMNet [4], Pix2Vox++ [55], and ONet [31]. Each of the approaches takes images as input. IMNet and ONet represent shapes implicitly using the occupancy function. Pix2Vox++ represents shapes as voxels. To adapt shape completion approaches for shape repair, we feed images of fractured objects as input and train each approach to predict the restoration shape. For IMNet we run their point sampling approach to sample voxels on the surface of each restoration shape at 16^3 , 32^3 , and 64^3 resolution. As done by the authors, we progressively train the IMNet auto-encoder at 16^3 , 32^3 , and 64^3 cubic resolution for 200, 200, and 400 epochs, and then train their single view reconstruction network for 1,000 epochs. For Pix2Vox++ we implement their 128^3 voxel resolution network, and train the network on 128^3 resolution voxelized restoration shapes for 250 epochs. For ONet, we use our point sampling approach to obtain 100,000 uniform and surface sampled points. We train ONet until the validation loss begins to decrease, i.e. for 255 epochs.

We show restoration shapes predicted by shape comple-

Class	IMNet				Pix2Vox++				ONet				Pix2Repair			
	CD	EMD	NC	NZ%	CD	EMD	NC	NZ%	CD	EMD	NC	NZ%	CD	EMD	NC	NZ%
airplane	0.082	0.078	0.536	91.80%	0.156	0.126	0.596	71.39%	0.047	0.044	0.651	97.76%	0.038	0.045	0.680	99.11%
bottle	0.011	0.016	0.613	100.00%	0.011	0.015	0.623	84.65%	0.004	0.007	0.657	100.00%	0.003	0.006	0.653	100.00%
car	0.068	0.069	0.643	99.09%	0.119	0.102	0.636	88.94%	0.044	0.042	0.777	100.00%	0.038	0.033	0.792	100.00%
chair	0.108	0.109	0.570	98.35%	0.208	0.169	0.547	57.39%	0.033	0.045	0.674	97.47%	0.032	0.044	0.702	100.00%
jar	0.034	0.044	0.565	100.00%	0.054	0.058	0.551	64.36%	0.023	0.028	0.612	98.55%	0.018	0.023	0.630	100.00%
mug	0.027	0.094	0.635	99.33%	0.040	0.122	0.610	79.53%	0.007	0.043	0.744	100.00%	0.005	0.047	0.750	99.66%
sofa	0.102	0.103	0.602	99.33%	0.323	0.285	0.568	68.23%	0.062	0.061	0.729	99.33%	0.046	0.052	0.749	100.00%
table	0.067	0.081	0.546	97.14%	0.100	0.104	0.523	59.30%	0.027	0.041	0.629	96.63%	0.029	0.048	0.652	100.00%
Mean	0.062	0.074	0.589	98.13%	0.126	0.123	0.582	71.72%	0.031	0.039	0.684	98.72%	0.026	0.037	0.701	99.85%

Table 2: Metrics for Pix2Repair and shape completion approaches adapted for repair. Means computed over classes. Best values bolded. We train one network over the entire dataset for each approach.

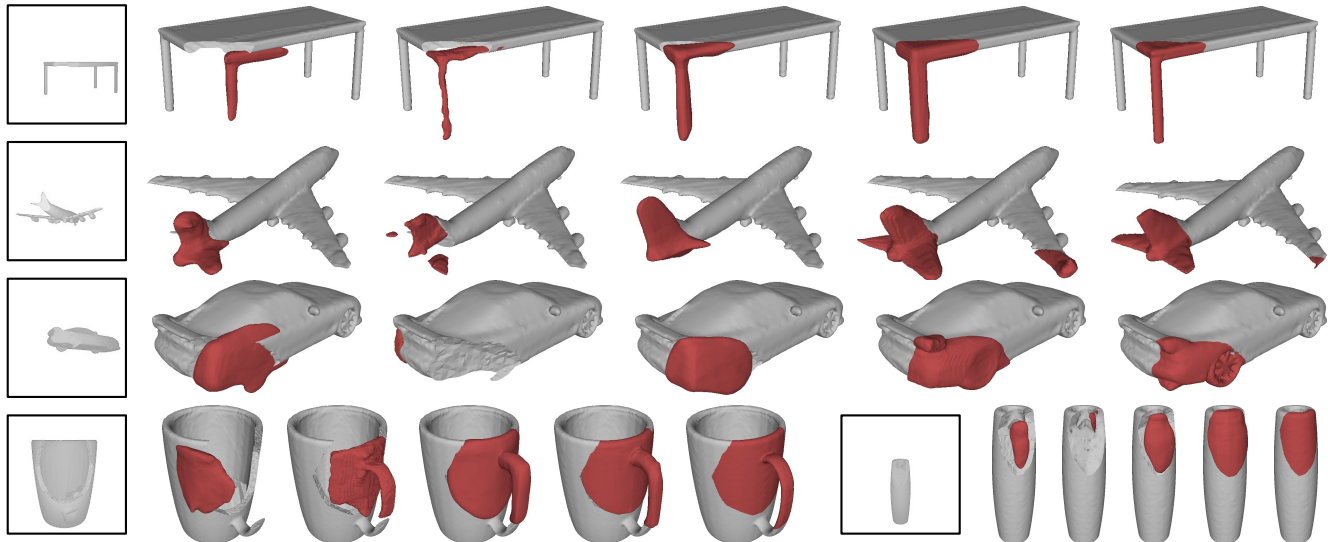


Figure 6: From left to right, input images, restorations using IMNet, Pix2Vox++, ONet, Pix2Repair, and ground truth.

tion approaches in Figure 6, and metrics in Table 2. Our approach outperforms shape completion approaches in terms of all metrics. ONet performs slightly worse than our approach in terms of all metrics, with a CD of 0.031 compared to 0.026, and EMD of 0.039 compared to 0.037. Restorations predicted by ONet are smoother than restorations using Pix2Repair, as shown in Figure 6. By representing the restoration shape as a Boolean intersection, our approach is able to generate restorations that connect tightly to the fractured shape, e.g. for the airplane and car in Figure 6. IMNet performs worse than ONet for all metrics, but outperforms Pix2Vox++. Though IMNet trains on voxelized sample points, they use a hierarchical sampling approach that samples more densely near the surface of shapes, enabling them to perform reasonably well on small restoration shapes. However, Pix2Vox++ predicts shape occupancy over a grid of discrete values which may not fall inside of the restoration shape. Due to the sparseness of restoration shapes, Pix2Vox++ struggles to generate accurate restorations, giving a low CD and EMD of 0.126 and

0.123, and fails to generate restorations in 28.28% of cases. Shape completion approaches often fail to generate small parts, such as the wingtip of the airplane in Figure 6.

6.3. View-Centered vs Object-Centered Repair

Our approach predicts restoration shapes in the canonical orientation, i.e. in an object-centered coordinate frame. As axially symmetric objects, such as the cup, bottle, and vase on the left of Figure 5, have multiple valid canonical orientations, they also have multiple valid object-centered restoration shapes, causing pose ambiguity in the predicted restoration shape. To overcome pose ambiguity, we train a version of our network that predicts view-centered restoration shapes, i.e. shapes in the coordinate frame of the camera instead of the object. View-centered restorations have a single valid restoration shape for axially symmetric objects. Though view-centered predictions have been shown to increase network generalizability [43], the task is also more challenging [55]. We train view-centered networks on the jars, mugs, and airplanes classes from Geometric Breaks.

Class	View Centered		Object Centered		
	CD _{nr}	NZ%	CD _{nr}	CD	NZ%
mugs	0.0232	96.98%	0.0276	0.0096	100.00%
jars	0.0301	98.55%	0.0695	0.0159	98.91%
airplanes	0.0747	86.44%	0.0314	-	99.40%

Table 3: Metrics for object-centered and view-centered repair using Pix2Repair. CD_{nr} indicates chamfer without a rotation about the up-axis. Best values bolded.

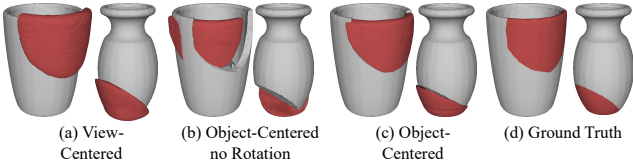


Figure 7: View-centered restorations, and object-centered restoration shapes before and after corrective rotation.

We show CD and NZ% for view and object-centered restorations in Table 3. For object-centered restorations we compute chamfer without rotation (CD_{nr}) and with rotation (CD) about the up-axis for jars and mugs. We perform the rotation to account for incorrect pose, as described in Section 6. We do not perform a rotation for view-centered restorations. As shown in Table 3, view-centered CD_{nr}, i.e. CD before corrective rotation, is less than object-centered CD_{nr} for mugs and jars, with 0.0232 compared to 0.0276 for mugs and 0.0301 compared to 0.0695 for jars. However, correcting the restoration shape pose by performing a rotation reduces the CD to 0.0096 and 0.0159 for mugs and jars, as shown in column 4 of Table 3. The reduction indicates object-centered shapes are more accurate than view-centered shapes, though their predicted pose may be incorrect. As shown in Figure 7(a), view-centered restorations show the correct pose, but are less accurate than object-centered restorations after rotation, as shown in Figure 7(c).

Airplanes do not exhibit axial symmetry and are not improved in terms of CD_{nr} when using view-centered restorations, as the object-centered restoration pose for airplanes is typically correct. View-centered restorations reconstruct fewer shapes than object-centered restorations, as shown in columns 2 and 5 of Table 3, indicating the difficulty of view-centered repair. Though view-centered repairs are less accurate, knowing the shape pose enables other applications to use the pose of the predicted restoration shape as input, e.g. for grasping algorithms such as GraspNet [7].

7. Conclusion

We present Pix2Repair, an approach to automatically generate restoration shapes from images. Our approach outperforms existing shape completion approaches adapted for shape repair. Though Pix2Repair is trained on objects

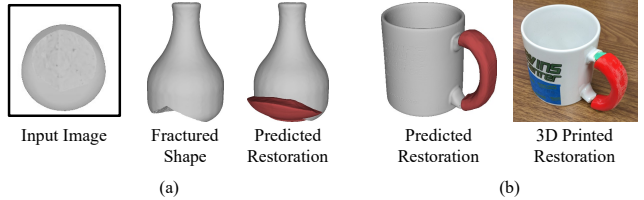


Figure 8: (a) Single view images may not provide enough information. (b) 3D printed repairs must be re-scaled.

from ShapeNet, it generalizes well to repairing objects from other datasets, including cultural heritage objects from the QP dataset, and physically fractured and scanned real objects. In contrast to existing approaches that require high-resolution 3D models, by operating on images of fractured objects Pix2Repair represents a significant step forward in increasing the accessibility of repair algorithms.

One limitation of our approach is that a single image of the fractured object may not observe parts of the object that are essential to determining its overall structure, as occurs in Figure 8(a). Single image perspectives are also made more challenging by flat lighting. Flat lighting may occur in our renders, e.g., Figure 8(a) as we render objects using a spotlight at the camera center. Object repair algorithms must be robust to the variety of camera angles and lighting conditions that may occur in the wild. As part of future work we will investigate adding a multi-view component to our approach, allowing users to input images of an object from different perspectives to increase restoration accuracy.

Another limitation is that restoration shapes predicted by our approach are not accurate to scale, preventing them from being used directly for 3D printing. It is not possible to accurately determine object scale from color images without external information. We manually re-scale, 3D print, and attach a predicted restoration shape to a fractured object with putty in Figure 8(b). Re-scaling may inhibit the restoration part from fitting snugly. As part of future work we will explore predicting restoration shapes from other modalities that include scale information, i.e. depth images.

Though neither Geometric Breaks or Breaking Bad contain textures, as part of future work will investigate transferring textures to objects from these datasets. Texture may help differentiate the fractured region from the intact region of the fractured shape. To increase the robustness of our approach to real images, we will follow work in learning from synthetic data [45, 8] and composite our fractured renders with real images to simulate realistic environments. We are currently collecting a dataset of images with pose annotations of real fractured objects in a variety of locations. Our image dataset will enable training shape repair approaches to repair real fractures in the wild, marking an important step towards realizing accessible and democratized repair.

References

- [1] Kaja Antlej, Miran Eric, Mojca Savnik, Bernarda Zupanek, Janja Slabe, and B Borut Battestin. Combining 3d technologies in the field of cultural heritage: Three case studies. In *VAST (Short and Project Papers)*, 2011. [2](#)
- [2] Jonathan M Bekisz, Hannah A Liss, Samantha G Maliha, Lukasz Witek, Paulo G Coelho, and Roberto L Flores. In-house manufacture of sterilizable, scaled, patient-specific 3d-printed models for rhinoplasty. *Aesthetic Surgery Journal*, 39(3):254–263, 2019. [2](#)
- [3] Angel X. Chang, Thomas Funkhouser, Leonidas Guibas, Pat Hanrahan, Qixing Huang, Zimo Li, Silvio Savarese, Manolis Savva, Shuran Song, Hao Su, Jianxiong Xiao, Li Yi, and Fisher Yu. ShapeNet: An Information-Rich 3D Model Repository. Technical Report arXiv:1512.03012 [cs.GR], Stanford University — Princeton University — Toyota Technological Institute at Chicago, 2015. [2, 4](#)
- [4] Zhiqin Chen and Hao Zhang. Learning implicit fields for generative shape modeling. In *Proc. CVPR*, pages 5939–5948, Piscataway, NJ, 2019. IEEE. [1, 3, 5, 6](#)
- [5] Christopher B Choy, Danfei Xu, JunYoung Gwak, Kevin Chen, and Silvio Savarese. 3d-r2n2: A unified approach for single and multi-view 3d object reconstruction. In *European conference on computer vision*, pages 628–644. Springer, 2016. [3](#)
- [6] Angela Dai, Christian Diller, and Matthias Nießner. Sg-nn: Sparse generative neural networks for self-supervised scene completion of rgb-d scans. In *Proceedings of the IEEE/CVF Conference on Computer Vision and Pattern Recognition*, pages 849–858, 2020. [3](#)
- [7] Hao-Shu Fang, Chenxi Wang, Minghao Gou, and Cewu Lu. Grasnet-1billion: A large-scale benchmark for general object grasping. In *Proceedings of the IEEE/CVF conference on computer vision and pattern recognition*, pages 11444–11453, 2020. [8](#)
- [8] Georgios Georgakis, Arsalan Mousavian, Alexander C Berg, and Jana Kosecka. Synthesizing training data for object detection in indoor scenes. *arXiv preprint arXiv:1702.07836*, 2017. [8](#)
- [9] Georgia Gkioxari, Jitendra Malik, and Justin Johnson. Mesh r-cnn. In *Proceedings of the IEEE/CVF International Conference on Computer Vision*, pages 9785–9795, 2019. [2](#)
- [10] Thibault Groueix, Matthew Fisher, Vladimir G Kim, Bryan C Russell, and Mathieu Aubry. A papier-mâché approach to learning 3d surface generation. In *Proc. CVPR*, pages 216–224, Piscataway, NJ, 2018. IEEE. [2](#)
- [11] Madan M Gupta and J11043360726 Qi. Theory of t-norms and fuzzy inference methods. *Fuzzy sets and systems*, 40(3):431–450, 1991. [3](#)
- [12] Renato Hermoza and Ivan Sipiran. 3d reconstruction of incomplete archaeological objects using a generative adversarial network. In *Proceedings of Computer Graphics International*, pages 5–11. ACM, New York, NY, 2018. [1, 2](#)
- [13] Zixuan Huang, Stefan Stojanov, Anh Thai, Varun Jampani, and James M Rehg. Planes vs. chairs: Category-guided 3d shape learning without any 3d cues. In *European Conference on Computer Vision*, pages 727–744. Springer, 2022. [5](#)
- [14] Ka-Hei Hui, Ruihui Li, Jingyu Hu, and Chi-Wing Fu. Neural template: Topology-aware reconstruction and disentangled generation of 3d meshes. In *Proceedings of the IEEE/CVF Conference on Computer Vision and Pattern Recognition*, pages 18572–18582, 2022. [1, 3, 5](#)
- [15] Sergey Ioffe and Christian Szegedy. Batch normalization: Accelerating deep network training by reducing internal covariate shift. In *International conference on machine learning*, pages 448–456. pmlr, 2015. [4](#)
- [16] Diederik P Kingma and Jimmy Ba. Adam: A method for stochastic optimization. In *Proc. ICLR*, pages 1–15, La Jolla, CA, 2014. International Conference on Representation Learning. [4](#)
- [17] Anestis Koutsoudis, George Pavlidis, Fotis Arnaoutoglou, Despina Tsiafakis, and Christodoulos Chamzas. Qp: A tool for generating 3d models of ancient greek pottery. *Journal of Cultural Heritage*, 10(2):281–295, 2009. [2, 4](#)
- [18] Nikolas Lamb, Sean Banerjee, and Natasha Kholgade Banerjee. Automated reconstruction of smoothly joining 3d printed restorations to fix broken objects. In *Proc. SCF*, pages 1–12, New York, NY, 2019. ACM. [2](#)
- [19] Nikolas Lamb, Sean Banerjee, and Natasha Kholgade Banerjee. Deepjoin: Learning a joint occupancy, signed distance, and normal field function for shape repair. *ACM Transactions on Graphics (TOG)*, 41(6):1–10, 2022. [1, 2, 4](#)
- [20] Nikolas Lamb, Sean Banerjee, and Natasha Kholgade Banerjee. Deepmend: Learning occupancy functions to represent shape for repair. In *European Conference on Computer Vision*, pages 433–450. Springer, 2022. [1, 2, 3](#)
- [21] Nikolas Lamb, Sean Banerjee, and Natasha K. Banerjee. MendNet: Restoration of Fractured Shapes Using Learned Occupancy Functions. *Computer Graphics Forum*, 2022. [1, 2](#)
- [22] Nikolas Lamb, Cameron Palmer, Ben Molloy, Sean Banerjee, and Natasha Kholgade Banerjee. Fantastic breaks: A dataset of paired 3d scans of real-world broken objects and their complete counterparts. In *Proceedings of the IEEE conference on computer vision and pattern recognition*, 2023. [2, 4](#)
- [23] Er Li, Xiaopeng Zhang, and Yanyun Chen. Symmetry based chinese ancient architecture reconstruction from incomplete point cloud. In *2014 5th International conference on digital home*, pages 157–161. IEEE, 2014. [2](#)
- [24] Manyi Li and Hao Zhang. D2im-net: Learning detail disentangled implicit fields from single images. In *Proceedings of the IEEE/CVF Conference on Computer Vision and Pattern Recognition*, pages 10246–10255, 2021. [1, 3](#)
- [25] Chen-Hsuan Lin, Chaoyang Wang, and Simon Lucey. Sdf-srn: Learning signed distance 3d object reconstruction from static images. *arXiv preprint arXiv:2010.10505*, 1(1):1–17, 2020. [1, 3](#)
- [26] Minghua Liu, Lu Sheng, Sheng Yang, Jing Shao, and Shi-Min Hu. Morphing and sampling network for dense point cloud completion. In *Proceedings of the AAAI Conference on Artificial Intelligence*, volume 34, pages 11596–11603, Menlo Park, CA, 2020. AAAI. [5](#)

[27] William E Lorensen and Harvey E Cline. Marching cubes: A high resolution 3d surface construction algorithm. *ACM SIGGRAPH Computer Graphics*, 21(4):163–169, 1987. 4

[28] Priyanka Mandikal, KL Navaneet, Mayank Agarwal, and R Venkatesh Babu. 3d-lmnet: Latent embedding matching for accurate and diverse 3d point cloud reconstruction from a single image. *arXiv preprint arXiv:1807.07796*, 2018. 2

[29] Matthew Matl. Pyrender, 2023. 5

[30] Pavlos Mavridis, Ivan Sipiran, Anthousis Andreadis, and Georgios Papaioannou. Object completion using k-sparse optimization. In *Computer Graphics Forum*, volume 34, pages 13–21. Wiley Online Library, 2015. 2

[31] Lars Mescheder, Michael Oechsle, Michael Niemeyer, Sebastian Nowozin, and Andreas Geiger. Occupancy networks: Learning 3d reconstruction in function space. In *Proc. CVPR*, pages 4460–4470, Piscataway, NJ, 2019. IEEE. 1, 3, 5, 6

[32] Kaichun Mo, Shilin Zhu, Angel X Chang, Li Yi, Subarna Tripathi, Leonidas J Guibas, and Hao Su. Partnet: A large-scale benchmark for fine-grained and hierarchical part-level 3d object understanding. In *Proceedings of the IEEE/CVF conference on computer vision and pattern recognition*, pages 909–918, 2019. 4

[33] Zak Murez, Tarrence Van As, James Bartolozzi, Ayan Sinha, Vijay Badrinarayanan, and Andrew Rabinovich. Atlas: End-to-end 3d scene reconstruction from posed images. In *European conference on computer vision*, pages 414–431. Springer, 2020. 1, 3

[34] Jeong Joon Park, Peter Florence, Julian Straub, Richard Newcombe, and Steven Lovegrove. Deepsdf: Learning continuous signed distance functions for shape representation. In *Proc. CVPR*, pages 165–174, Piscataway, NJ, 2019. IEEE. 2, 5

[35] Guiju Ping, Mahdi Abolfazli Esfahani, Jiaying Chen, and Han Wang. Visual enhancement of single-view 3d point cloud reconstruction. *Computers & Graphics*, 102:112–119, 2022. 2

[36] Stefan Popov, Pablo Bauszat, and Vittorio Ferrari. Corenet: Coherent 3d scene reconstruction from a single rgb image. In *European Conference on Computer Vision*, pages 366–383. Springer, 2020. 3

[37] Fabian Rengier, Amit Mehndiratta, Hendrik Von Tengg-Kobligk, Christian M Zechmann, Roland Unterhinninghofen, H-U Kauczor, and Frederik L Giesel. 3d printing based on imaging data: review of medical applications. *International journal of computer assisted radiology and surgery*, 5(4):335–341, 2010. 2

[38] René Schilling, Benjamin Jastram, Oliver Wings, Daniela Schwarz-Wings, and Ahi Sema Issever. Reviving the dinosaur: virtual reconstruction and three-dimensional printing of a dinosaur vertebra. *Radiology*, 270(3):864–871, 2014. 2

[39] Roberto Scopigno, Marco Callieri, Paolo Cignoni, Massimiliano Corsini, Matteo Dellepiane, Federico Ponchio, and Guido Ranzuglia. 3d models for cultural heritage: Beyond plain visualization. *Computer*, 44(7):48–55, 2011. 2

[40] Maria Luiza Seixas, Paulo Santos Assis, João Cura D’Ars Figueiredo, Maria Aparecida Pinto, and Daniella Gualberto Caldeira Paula. The use of rapid prototyping in the joining of fractured historical silver object. *Rapid Prototyping Journal*, 2018. 2

[41] S. Sellán, Y. Chen, Z. Wu, A. Garg, and A. Jacobson. Breaking bad: A dataset for geometric fracture and reassembly. In *Thirty-sixth Conference on Neural Information Processing Systems Datasets and Benchmarks Track*, 2022. 2, 4

[42] Yue Shi, Bingbing Ni, Jinxian Liu, Dingyi Rong, Ye Qian, and Wenjun Zhang. Geometric granularity aware pixel-to-mesh. In *Proceedings of the IEEE/CVF International Conference on Computer Vision*, pages 13097–13106, 2021. 2

[43] Daeyun Shin, Charless C Fowlkes, and Derek Hoiem. Pixels, voxels, and views: A study of shape representations for single view 3d object shape prediction. In *Proceedings of the IEEE conference on computer vision and pattern recognition*, pages 3061–3069, 2018. 7

[44] Ivan Sipiran. Completion of cultural heritage objects with rotational symmetry. In *Proceedings of the 11th Eurographics Workshop on 3D Object Retrieval*, pages 87–93, 2018. 2

[45] Shashank Tripathi, Siddhartha Chandra, Amit Agrawal, Ambish Tyagi, James M Rehg, and Visesh Chari. Learning to generate synthetic data via compositing. In *Proceedings of the IEEE/CVF Conference on Computer Vision and Pattern Recognition*, pages 461–470, 2019. 8

[46] Nanyang Wang, Yinda Zhang, Zhuwen Li, Yanwei Fu, Wei Liu, and Yu-Gang Jiang. Pixel2mesh: Generating 3d mesh models from single rgb images. In *Proceedings of the European conference on computer vision (ECCV)*, pages 52–67, 2018. 2

[47] Weiyue Wang, Duygu Ceylan, Radomir Mech, and Ulrich Neumann. 3dn: 3d deformation network. In *Proceedings of the IEEE/CVF Conference on Computer Vision and Pattern Recognition*, pages 1038–1046, 2019. 2

[48] Yujie Wang, Yixin Zhuang, Yunzhe Liu, and Baoquan Chen. Mdisn: Learning multiscale deformed implicit fields from single images. *Visual Informatics*, 2022. 1, 3

[49] Jiajun Wu, Yifan Wang, Tianfan Xue, Xingyuan Sun, Bill Freeman, and Josh Tenenbaum. Marrnet: 3d shape reconstruction via 2.5 d sketches. *Advances in neural information processing systems*, 30, 2017. 3

[50] Jiajun Wu, Chengkai Zhang, Xiuming Zhang, Zhoutong Zhang, William T Freeman, and Joshua B Tenenbaum. Learning shape priors for single-view 3d completion and reconstruction. In *Proceedings of the European Conference on Computer Vision (ECCV)*, pages 646–662, 2018. 2

[51] Rundi Wu, Yixin Zhuang, Kai Xu, Hao Zhang, and Baoquan Chen. Pq-net: A generative part seq2seq network for 3d shapes. In *Proceedings of the IEEE/CVF Conference on Computer Vision and Pattern Recognition*, pages 829–838, 2020. 2

[52] Tong Wu, Liang Pan, Junzhe Zhang, Tai Wang, Ziwei Liu, and Dahua Lin. Density-aware chamfer distance as a comprehensive metric for point cloud completion. *arXiv preprint arXiv:2111.12702*, 2021. 5

- [53] Tong Wu, Jiaqi Wang, Xingang Pan, Xudong Xu, Christian Theobalt, Ziwei Liu, and Dahua Lin. Voxurf: Voxel-based efficient and accurate neural surface reconstruction. *arXiv preprint arXiv:2208.12697*, 2022. 3
- [54] Haozhe Xie, Hongxun Yao, Xiaoshuai Sun, Shangchen Zhou, and Shengping Zhang. Pix2vox: Context-aware 3d reconstruction from single and multi-view images. In *Proceedings of the IEEE/CVF international conference on computer vision*, pages 2690–2698, 2019. 3
- [55] Haozhe Xie, Hongxun Yao, Shengping Zhang, Shangchen Zhou, and Wenxiu Sun. Pix2vox++: Multi-scale context-aware 3d object reconstruction from single and multiple images. *International Journal of Computer Vision*, 128(12):2919–2935, 2020. 3, 6, 7
- [56] Yifan Xu, Tianqi Fan, Yi Yuan, and Gurprit Singh. Ladybird: Quasi-monte carlo sampling for deep implicit field based 3d reconstruction with symmetry. In *European Conference on Computer Vision*, pages 248–263. Springer, 2020. 1, 3
- [57] Li Yi, Boqing Gong, and Thomas Funkhouser. Complete & label: A domain adaptation approach to semantic segmentation of lidar point clouds. In *Proceedings of the IEEE/CVF Conference on Computer Vision and Pattern Recognition*, pages 15363–15373, 2021. 3
- [58] Qian Yu, Chengzhan Yang, and Hui Wei. Part-wise atlasnet for 3d point cloud reconstruction from a single image. *Knowledge-Based Systems*, page 108395, 2022. 2
- [59] Qingnan Zhou and Alec Jacobson. Thingi10k: A dataset of 10,000 3d-printing models. *arXiv preprint arXiv:1605.04797*, 2016. 4